

Design and fabrication of a pixel polarizer array at 700–900 nm wavelength

ZHENDUO ZHANG^{a,b}, ZHANJUN MA^{a,b}, ZEXI LIU^c, WANPENG ZHAO^d, ZIJIAN WANG^d, YUBO LI^{d,e,*}

^aNavigation College, Dalian Maritime University, Dalian 116026, China

^bEnvironmental Information Institute, Dalian Maritime University, Dalian 116026, China

^cCollege of Engineering, University of California Santa Barbara, Santa Barbara 93106, United States of America

^dInformation Science and Electronic Engineering College, Zhejiang University, Hangzhou 310027, China

^eResearch Institute of Zhejiang University-Shenzhen, Shenzhen 518057, China

For polarization imaging, the wire-grid polarizer is one of the most popular devices. We designed and fabricated a pixel polarizer array (PPA) based on a wire-grid polarizer at 700–900 nm wavelength. We studied the influence of different structural parameters on the extinction ratio and transverse magnetic (TM) mode transmissivity of the system. Simulations of the PPA performance using the optimal structure were conducted and a complete PPA fabrication flow was introduced. The polarization characteristics and appearance of the PPA was observed using polarizing and scanning electron microscopies, which preliminarily confirm the accuracy of the design results and the feasibility of the processing technology.

(Received June 9, 2020; accepted June 11, 2021)

Keywords: Pixel polarizer array, Polarization technology, Wire grid, Extinction ratio

1. Introduction

Polarization, inherent property of light, represents an optical information dimension that is independent of intensity, wavelength, and coherence; it reflects the optical characteristics of a target from a new perspective. If polarization is combined with other features such as intensity, spectrum, and image, its attributes and behaviors can be more accurately understood because multiple dimensions of optical information are used together to represent the same target [1–7]. Polarization technology has been extensively applied for various target imaging detection fields. Time-sharing, separate amplitude, separate aperture, and separate focal plane type (SFT) polarizations are the different types of polarization optical imaging detection systems [8–10]. In the polarization imaging detection method, SFT polarization is a breakthrough, showing the advantages of good real-time imaging, small volume and mass, and compact structure. Moreover, the SFT optical system can simultaneously detect the target light information in four different polarization directions and obtain the intensity image, polarization-degree image, and polarization-angle image of the target. SFT polarization has been extensively used in microscopy, atmospheric monitoring, aviation and space target detection, and remote sensing [11–16]. For realizing SFT, two optical path structures are used: i) to integrate a pixel polarizer array (PPA) to form a polarizer array detector at a micro-distance before the conventional detector and ii) to use the principle of secondary imaging to place the PPA at the middle image plane of the optical system. PPA is the key component of the SFT optical system, regardless of the optical path structure. Therefore, the design and fabrication of PPAs has recently become a

hot issue [17–22]. For the 700–900-nm wavelength range, PPA can be used in numerous applications to further improve the resolution and recognition ability of the target, such as transparent fog detection, fluorophores for biomedical imaging, and high-resolution imaging of space targets [23–30]; however, there are very few reports on the special design and fabrication of PPAs at 700–900 nm.

In this study, we designed and fabricated a PPA based on a wire-grid polarizer at a wavelength of 700–900 nm. Section 2 presents the theoretical basis of design for the PPA. The metal-grating material, grating pitch, grating width, and grating height were analyzed and determined, and the performance of the PPA was simulated in Section 3. Section 4 shows the fabrication flow and the overall appearance and polarization characteristics of PPA. Section 5 shows that the design results agree with technical specifications; moreover, the scope for a future research work is also discussed in this section.

2. Theoretical basis of pixel polarizer array design

For developing more reliable and compact devices, PPAs are developed using nano-fabrication techniques and adjusted to be of “transmission type”. Fig. 1(a) shows the parameters and structures of the PPAs. The metal grating was fabricated on a substrate, e.g., silicon oxide sheet, which offers high transparent for 700–900-nm wavelength. The metal-grating parameters include the material, height (h), width (w), pitch (s), period (p) parameters, and duty cycle ($a = w/p$). Figure 1(b) shows the layout of the wire grid and the polarization characteristics of the PPA for an unpolarized electromagnetic wave at normal incidence. The wire grid is periodically arranged along the

X axis and the length direction is parallel to the Y axis. The transverse magnetic (TM) and transverse electric (TE) modes show electromagnetic waves whose electric-field vectors are parallel to the X and Y axes, respectively. The subwavelength metal grating allows most of the TM-polarized light to pass through but strongly reflects the TE polarized one, acting as a linear polarizer rather than a diffraction grating.

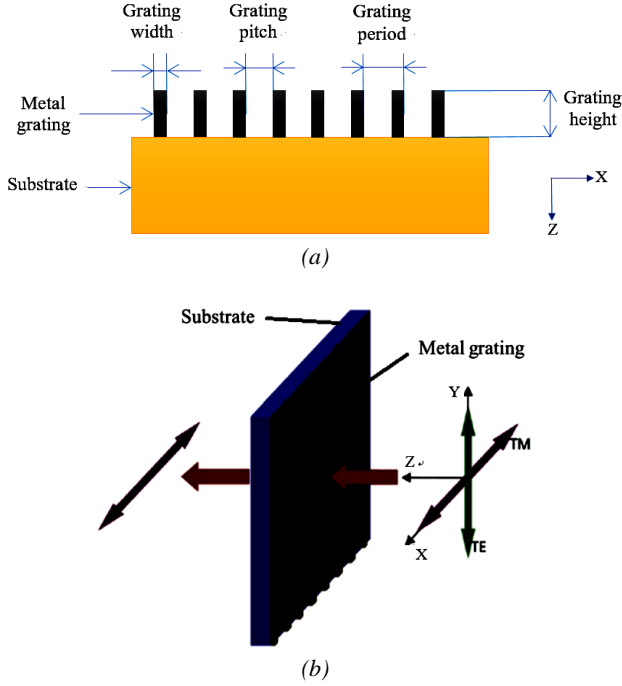


Fig. 1. (a) Plane diagram and (b) three-dimensional diagram of the PPA parameters and structure (color online)

TM transmissivity (TMT) and extinction ratio (ER) are the two most important parameters for evaluating the performance of PPA. ER is the ratio of the TMT to TE transmissivity (TET) of PPA, expressed as:

$$ER = 10 \log_{10} \left(\frac{TMT}{TET} \right) \quad (1)$$

When the grating period is greater than the incident light wavelength, since the grating has multi-order diffracted waves, the grating can only be used as a diffraction grating, not as a polarizer. When the period of the grating is close to the incident wavelength, the grating is in the resonance region, and its reflectivity and transmittance will change drastically. This phenomenon is called Rayleigh anomalies [31]. When the grating period is much smaller than the incident light wavelength, the grating has only zero-order diffraction wave, the equivalent refractive index of the sub-wavelength metal grating can be approximately calculated using the equivalent medium theory, and the polarization characteristics of the metal grating can be analyzed. By solving the boundary conditions of Maxwell's equations, the equivalent refractive index of TM-polarized light

n_{TM} and TE-polarized light n_{TE} on subwavelength metal gratings can be obtained [32]:

$$n_{TM} = \frac{1}{\sqrt{an_M^{-2} + (1-a)n_s^{-2}}} \quad (2)$$

$$n_{TE} = \sqrt{an_M^2 + (1-a)n_s^2} \quad (3)$$

where n_M is the refractive index of the metal material and n_s is the refractive index of the substrate material. According to the rigorous coupled-wave theory (RCWA) [33], the Y electric field component of the electromagnetic wave in the grating region (in Fig. 1(b), the Y direction is perpendicular to the cross-section) can be written as:

$$E_Y = \sum_{i=0}^n T_i \exp\{-j[k_x x - k_z(z-h)]\} \quad (4)$$

where T_i represents the transmission amplitude corresponding to the i th-order diffraction electromagnetic wave and k_x and k_z correspond to the wave vector components in the X and Z directions in Fig. 1, respectively. k_x and k_z are expressed as:

$$k_x = k_0 \left(\sin \theta - \frac{i\lambda}{p} \right) \quad (5)$$

$$k_z = \begin{cases} +k_0 \sqrt{n_M^2 - \left(\frac{k_x}{k_0}\right)^2} & n_M > \frac{k_x}{k_0} \\ -jk_0 \sqrt{\left(\frac{k_x}{k_0}\right)^2 - n_M^2} & n_M < \frac{k_x}{k_0} \end{cases} \quad (6)$$

where k_0 is the wave vector of the incident light in vacuum. By solving the magnetic field component of the Maxwell equation, the diffraction efficiency of the TM mode can be finally obtained as:

$$\eta_{TM} = |T_i|^2 \operatorname{Re} \left(\frac{k_z}{k_0 \cos \theta} \right) \quad (7)$$

From Eq. (7), we can find that the TM diffraction efficiency can be effectively improved by adjusting T_i and k_z . Because the TMT and ER values are positively correlated with TM diffraction efficiency, we need to optimize the selection of the metal material and geometric parameters of the metal grating to obtain high polarization performance of PPA.

3. Pixel polarizer array design

We used the ER and TMT parameters to evaluate the performance of the PPA. Previous studies show that increasing the ER value when it is greater than 16.5 dB only has a small effect on the polarization-imaging accuracy of the system [34]. To guarantee a good fabrication performance of the PPA, the design index of this study is that the ER value should be higher than 20 dB and the TMT should be higher than 80%. This will be realized by designing various wire-grid parameters for the PPA.

3.1. Metal-grating material and pitch

Based on theory of finite difference time domain (FDTD) of vector electromagnetic wave, for the 700–900-nm wavelength, the ER characteristics of Al, Ag, and Au under different grating pitches were simulated. The substrate was an optical parallel plate made of silicon dioxide; the substrate thickness was 2 mm, the duty cycle was 50%, and the grating height was 100 nm. Fig. 2 shows the ER simulation results and Table 1 shows the corresponding ER value range. The ER value of Al, which has the highest ER at a grating pitch of 100 nm, is better than that of the other metal materials.

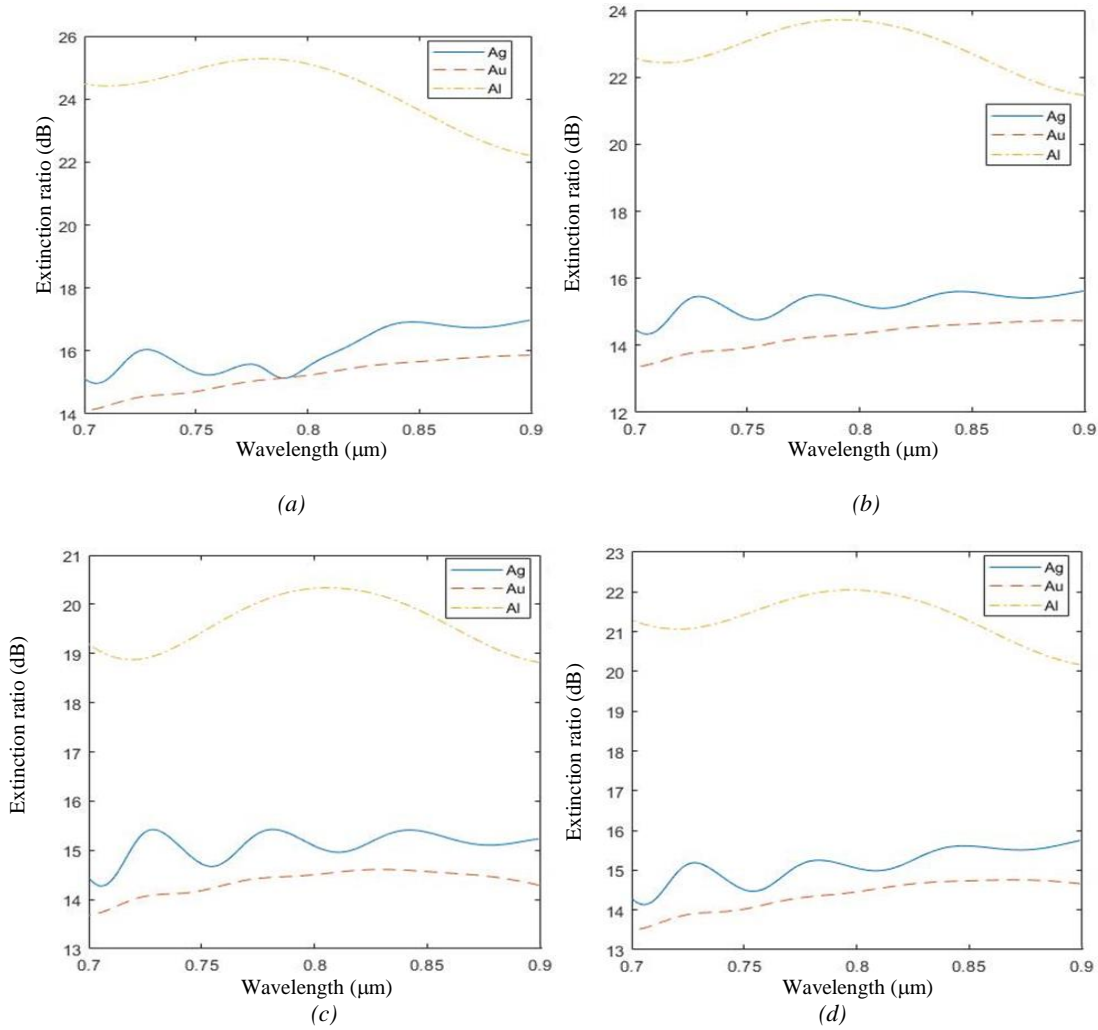


Fig. 2. FDTD simulation of the ER results for different metal materials and grating pitches in the case of (a) 100, (b) 110, (c) 120, and (d) 130 nm (color online)

Table 1. ER value range of different metal materials and grating pitches

Grating pitch	ER value range		
	Al	Ag	Au
100 nm	[22.2, 24.5] dB	[14.1, 15.9] dB	[15.1, 17.0] dB
110 nm	[21.5, 23.7] dB	[13.4, 14.7] dB	[14.3, 15.4] dB
120 nm	[20.2, 22.0] dB	[13.5, 14.8] dB	[14.1, 15.6] dB
130 nm	[18.8, 20.3] dB	[13.7, 14.6] dB	[14.3, 15.4] dB

3.2. Grating width

The ER and TMT characteristics for different grating widths were simulated at wavelengths of 700–900 nm. The grating pitch and the height were 100 and 160 nm, respectively. Fig. 3 shows the simulation results are shown in, where we can clearly observe the following points:

1. The ER value at short wavelengths is better than that at long wavelengths. If the wavelength is varied from 700 to 900 nm, the ER value first monotonically increases, then reaches a maximum (near 750 nm), and finally monotonically decreases. When the grating width is 44 nm, the ER value reaches the maximum in the whole range of 700–900 nm.
2. The TMT value monotonically decreases, and the longer the wavelength, the lower the TMT value. Furthermore, when the grating width is 40 nm, the TMT value reaches a maximum in the whole range of 700–900 nm. Note that the TMT value at a grating width 44 nm is 1.5% lower than that at 40 nm.

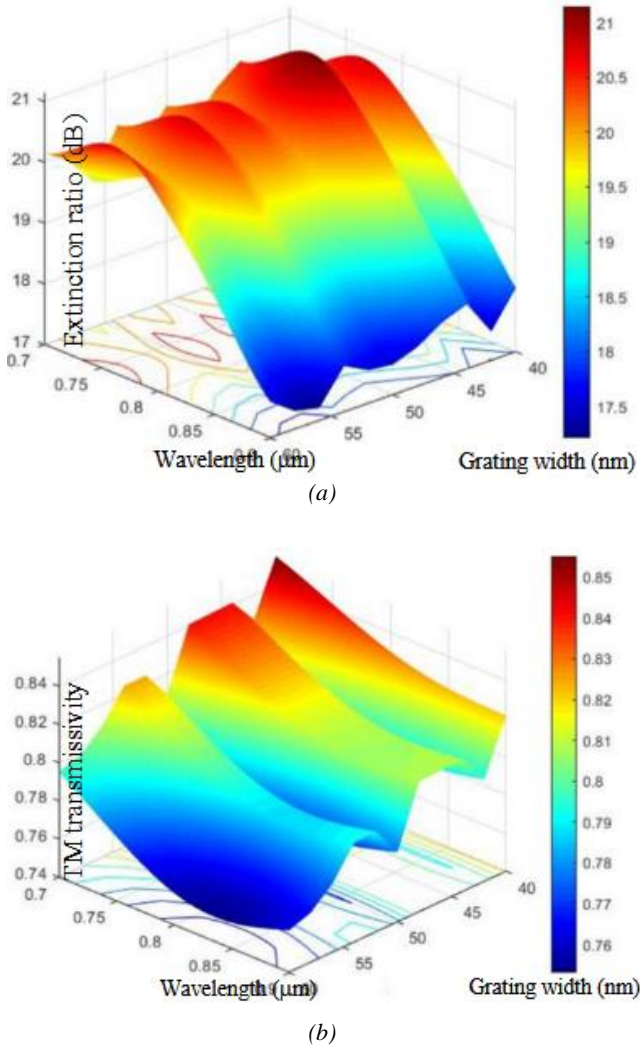


Fig. 3. (a) ER and (b) TMT simulation results for different grating widths (color online)

Considering that a wide grating width is conducive to ensuring a high machining accuracy, if there is only a small difference in TM transmissivity between grating widths of 40 and 44 nm, the 44-nm width (with higher ER value) was preliminarily selected as the fabrication parameter.

3.3. Grating height

Furthermore, the ER and TMT characteristics were simulated for different grating heights. The grating pitch and width were 100 and 50 nm, respectively, and the simulation heights were 100, 120, 140, 160, 180, and 200 nm. Fig. 4 shows the simulation results where we can summarize the experimental results as follows:

1. For different grating heights, the ER value first monotonically increases with the wavelength to a maximum, then monotonically decreases to a minimum, and finally increases again monotonically. The higher the grating height, the longer the wavelength corresponding to both maximum and minimum.
2. For grating heights of 100, 120, and 140 nm, the TMT value decreases with increasing wavelength. For grating heights of 160, 180, and 200 nm, the TMT value monotonically decreases within the 700–850-nm wavelength range and then monotonously increases between 850 and 900 nm.

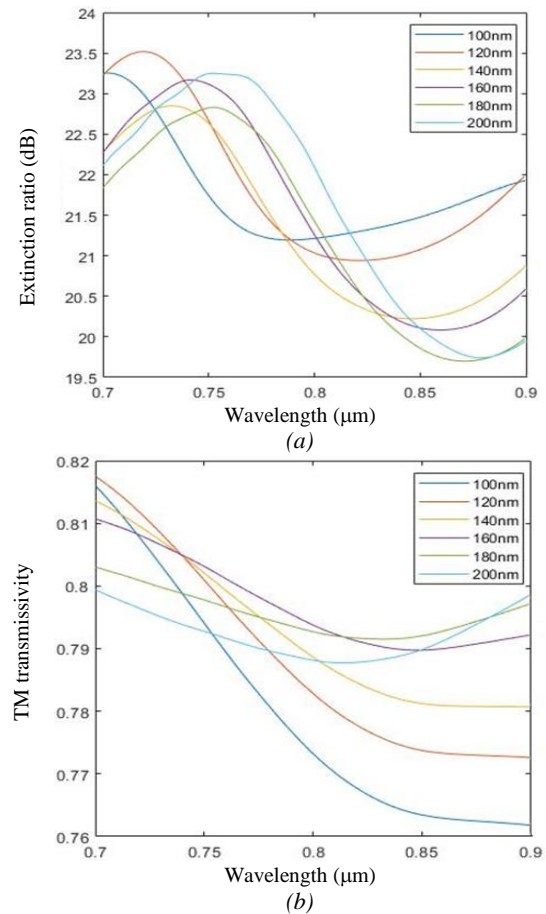


Fig. 4. (a) ER and (b) TMT simulation results for different grating heights (color online)

Considering that both ER and TMT values are good at a grating height of 120 nm and that a low grating height is conducive to ensuring a high machining accuracy, the height of 120 nm was preliminarily selected as the fabrication parameter.

3.4. Fine simulation of the PPA characteristics

The PPA fabrication parameters were selected based on the abovementioned optimization. These include Al as the metal-grating material, a grating pitch of 100 nm, a grating width of 44 nm, and a grating height of 120 nm. Fig. 5 shows the simulation results for the ER and TMT of the PPA in which we could clearly observe the following behavior:

1. The maximum ER value is ~ 24.2 dB at a wavelength close to 800 nm, and the minimum value is ~ 23.6 dB at a wavelength close to 700 and 900 nm. In the

wavelength range of 700–900 nm, the ER value is symmetrical.

2. The relationship between the TMT value and the wavelength shows a parabolic shape, which is axisymmetric when the wavelength is 800 nm. The TMT reaches a minimum value of $\sim 89.0\%$ at a wavelength close to 800 nm, a maximum value of $\sim 90.7\%$ at a wavelength of ~ 700 nm, and a high TMT value of 90.6% at a wavelength of ~ 900 nm.

3. Although the relationship between the ER and TMT values and the incident wavelength is complex in shape, the overall variation range is small (ER: [23.6–24.2 dB], TMT: [89.0%, 90.7%]). Therefore, the PPA prepared using these structure parameters is insensitive to the radiation wavelength. The design results completely meet the requirements of the design indicators.

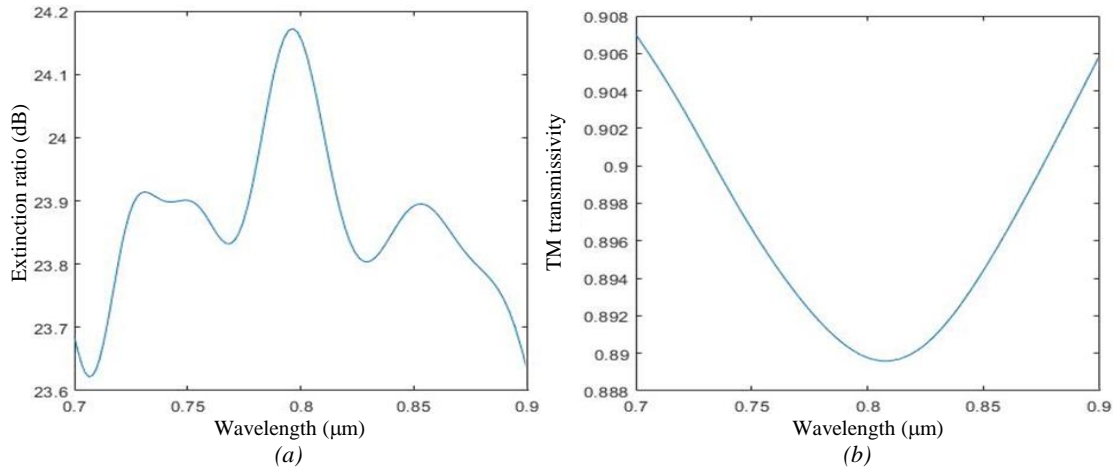


Fig. 5. (a) ER and (b) TMT simulation results for the PPA (color online)

4. PPA fabrication flow and results

The technology of electron beam exposure was adopted. Fig. 6 shows the specific fabrication flow is shown in. Considering the requirement for a conductive substrate for the electron beam exposure technology, the

PPA was fabricated by first coating the substrate with an Al film, then rotating the photoresist, followed by exposure, development, and metal etching.

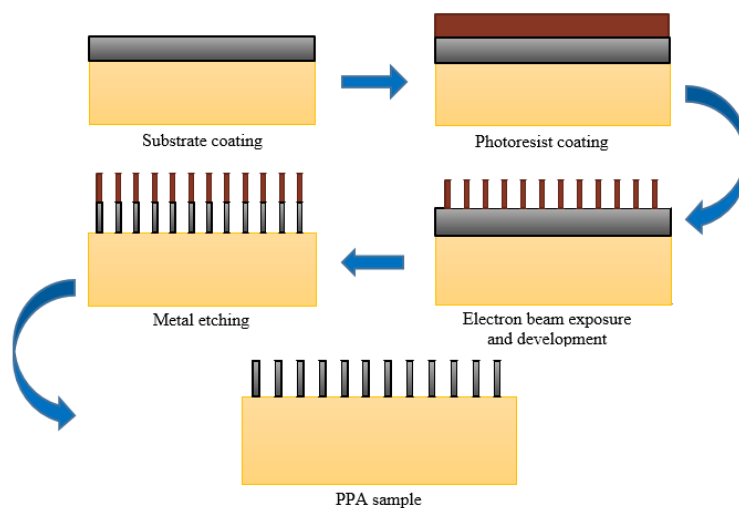


Fig. 6. The specific fabrication flow of PPA (color online)

Substrate coating was accomplished using magnetron sputtering vapor deposition. To prevent contamination from affecting the formation of the Al coating, the substrate was thoroughly cleaned before coating. Fig. 7 shows the coating results, and the surface of the parallel flat silicon dioxide plates forms a reflection mirror.

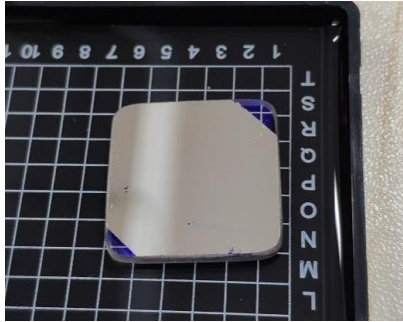


Fig. 7. Sample of an Al film obtained by magnetron sputtering (color online)

The RAITH150 two electron beam exposure system was used. Fig. 8 shows the layout of the PPA lithography, designed using L-Edit. A single polarization unit is composed of four polarization pixels in the polarization directions of 0° , 45° , 90° , and 135° , which is utilized to calculate the Stokes vectors. The size of each pixel is $13\ \mu\text{m} \times 13\ \mu\text{m}$ (including the spacing between pixels), and the size of the single polarization unit is $26\ \mu\text{m} \times 26\ \mu\text{m}$, as shown in Fig. 8(a). Fig. 8(b) shows the overall layout of the PPA. Since this is the first fabrication and considering the process time and cost, the fabrication size was selected as $2.6\ \text{mm} \times 2.6\ \text{mm}$.

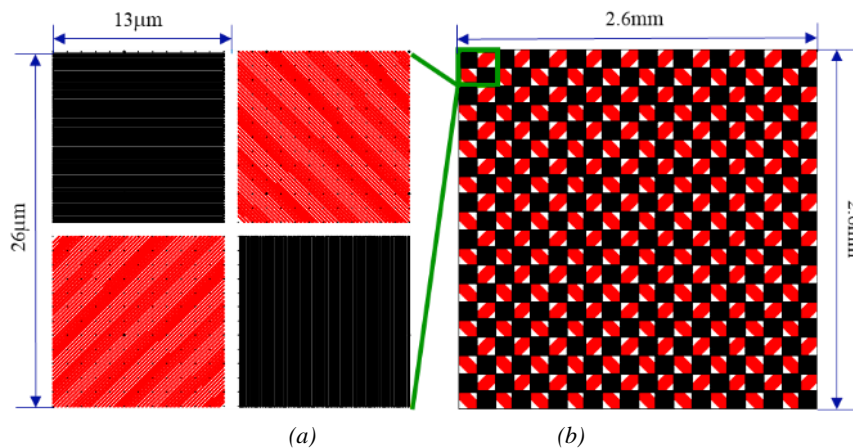


Fig. 8. The layout for lithography: (a) polarization pixel layout and (b) overall layout of the PPA (color online)

The PPA was prepared as per the abovementioned design parameters and fabrication flow. A scanning electron microscope was used to observe the fine appearance of the PPA at magnifications of about 3,000 and 10,000 times. Fig. 9 shows the observation results, and

the overall appearance of the grating is good; therefore, the feasibility of the fabrication technology and process has been preliminarily demonstrated.

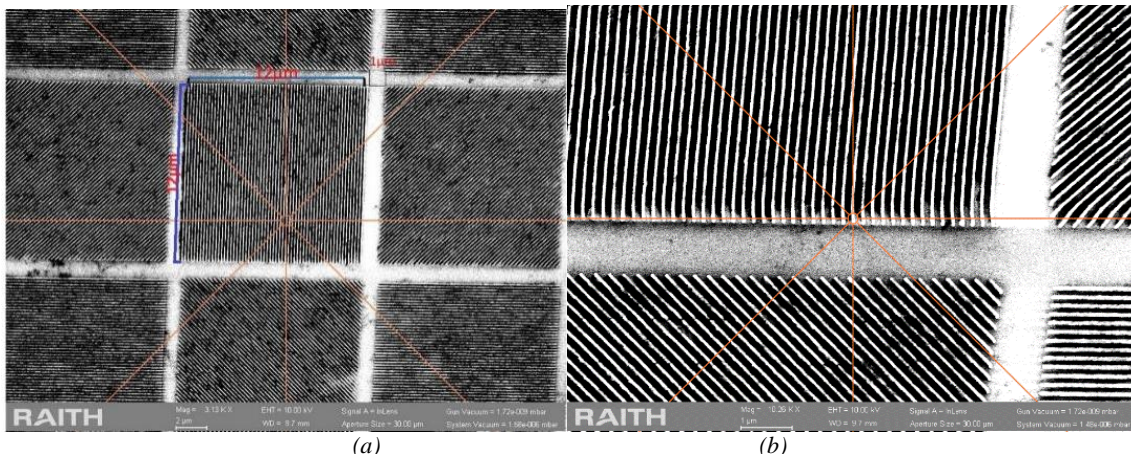


Fig. 9. SEM observation results at magnifications of about (a) 3,000 and (b) 10,000 times (color online)

The PPA was amplified by 50 and 100 times using a Nikon polarizing microscope and the polarization performance was preliminarily judged, as shown in Fig.10. For polarized incident light from the same beam, the PPA forms a total of four transmissivity values (different colors represent different TM transmissivity). The transmissivity values show a periodic distribution, which is similar to that of the polarization pixel layout, preliminarily proving the modulation effect of the PPA on the incident polarized light and the functional characteristics of the device.

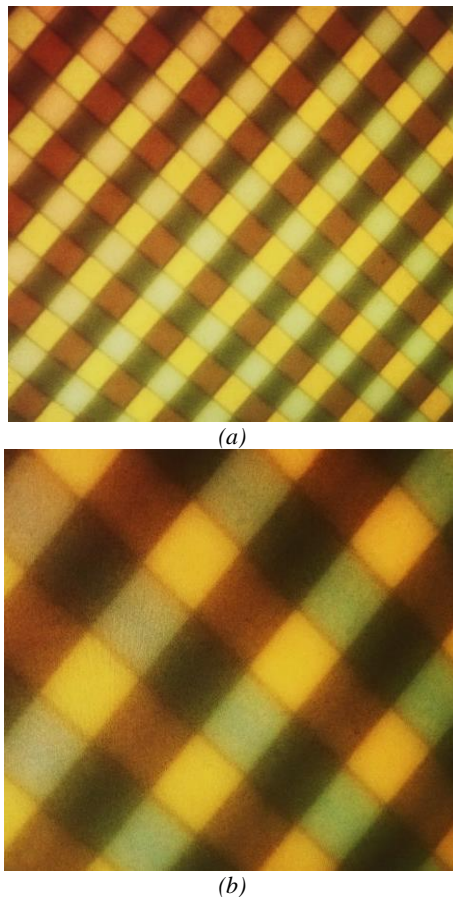


Fig. 10. Polarizing microscopy observation results at magnifications of (a) 50 times and (b) 100 times (color online)

5. Conclusion

Recently, the design and fabrication of PPAs has become a hot topic. Based on the theory of vector electromagnetic wave FDTD, this study analyzes the influences of the grating metal materials, grating pitch, grating width, and grating height on the ER and TMT values at 700–900 nm and obtains the optimal PPA design parameters. The performance simulation of the whole PPA is completed with ER values ranging from 23.6 to 24.2 dB and TMT values ranging from 89.0% to 90.7%. The design results completely meet the requirements of the design indicators. By using the electron beam exposure and magnetron sputtering coating technology, a PPA with a total size of 2.6×2.6 mm was fabricated. The feasibility

of the fabrication technology and flow, modulation effect, and functional characteristics of the PPA have been preliminarily demonstrated using observations by polarizing and scanning electron microscopy. Furthermore, based on the SFT method, the fabricated PPA will be used for polarization imaging. The polarization-direction information, measured simultaneously at 0° , 45° , 90° , and 135° , will be used to obtain intensity, polarization degree, and polarization-angle images of the target. The polarization performance of the PPA will be further confirmed and the polarization-imaging effect of the target will be studied. Next, we will complete the fabrication of a full-size PPA, which will eventually provide core hardware support for polarization detection technology based on the SFT method.

Acknowledgments

This work was financially supported by the National Key Research and Development Program of China (No. 2018YFB0406500), project No. 6141B06, Shenzhen science and technology bureau (No. JCYJ20180302150128636), and Fundamental Research Funds for the Central Universities (3132021137).

References

- [1] B. Kanseri, K. R. Sethuraj, *Opt. Lett.* **44**, 159 (2019).
- [2] N. Li, Y. Zhao, Q. Pan, S. G. Kong, *Opt. Express* **27**, 1376 (2019).
- [3] Z. Sun, D. Wu, Y. Lu, S. Lu, *IEEE T. Geosci. Remote Sens.* **57**, 4388 (2019).
- [4] L. Meng, J. P. Kerekes, *IEEE T. Geosci. Remote Sens.* **52**, 6615 (2014).
- [5] T. Hu, F. Shen, K. Wang, K. Guo, X. Liu, F. Wang, Z. Peng, Y. Cui, R. Sun, Z. Ding, J. Gao, Z. Guo, *Atmosphere* **10**, 342 (2019).
- [6] A.-L. Sahlberg, D. Hot, R. Lyngbye-Pedersen, J. Zhou, M. Ald, *Appl. Spectrosc.* **73**, 653 (2019).
- [7] M. Alizadeh, M. Ghotbi, P. Loza-Alvarez, D. Merino, *Methods Protoc.* **2**, 49 (2019).
- [8] L. Giudicotti, M. Brombin, *Appl. Opt.* **46**, 2638 (2007).
- [9] R. M. Matchko, G. Gerhart, *Opt. Eng.* **47**, 016001 (2008).
- [10] J. S. Tyo, D. L. Goldstein, D. B. Chenault, J. A. Shaw, *Appl. Opt.* **45**, 5453 (2006).
- [11] G. Myhre, Graham, W.-L. Hsu, A. Peinado, C. Lacasse, N. Brock, R. A. Chipman, S. Pau, *Opt. Express* **20**, 27393. (2012).
- [12] S. B. Powell, V. Gruev, *Opt. Express* **21**, 21039 (2013).
- [13] V. Gruev, R. Perkins, T. York, *Opt. Express* **18**, 19087 (2010).
- [14] M. Kulkarni, V. Gruev, *Opt. Express* **20**, 22997 (2012).
- [15] J. S. Tyo, C. F. LaCasse, B. M. Ratliff, *Opt. Lett.* **34**, 3187 (2009).
- [16] S. Gao, V. Gruev, *Opt. Express* **19**, 26161 (2011).

- [17] H. Yong, X. Shen, Y. Hu, M. Wang, Q. Zhang, Q. Zou, B. Li, Proceedings of the Institution of Mechanical Engineers, Part G: Journal of Aerospace Engineering **233**, 1916 (2019).
- [18] I. Yamada, Y. Ishihara Y, Appl. Phys. Express **9**, 052202 (2016).
- [19] I. Yamada, K. Kintaka, J. Nishii, S. Akioka, Y. Yamagishi, M. Saito, Opt. Lett. **33**, 258 (2008).
- [20] W. Zhi, P. E. Powers, A. M. Sarangan, Q. Zhan, Opt. Lett. **33**, 1653 (2008).
- [21] G. P. Nordin, J. T. Meier, P. C. Deguzman, M. W. Jones, J. Opt. Soc. Am. A **16**, 1168 (1999).
- [22] Y. Zhou, D. J. Klotzkin, Appl. Opt. **47**, 3555 (2008).
- [23] G. Hong, A. L. Antaris, H. Dai, Nat. Biomed. Eng. **1**, 1 (2017).
- [24] J. -L. Wang, Y. -L. Dong, K. N. Yao, X. -D. Lin, L.-Q. Yang, X.-Y. Liu, L. Wang, L. Chen, Opt. Prec. Eng. **26**, 1007 (2018).
- [25] X. D. Lin, X. -Y Liu, S. Wang, J. L. Wang, P. F. Wei, L. J. L. Jia, B. G. Chen, Z. Y. Wang, K. N. Yao, Opt. Prec. Eng. **24**, 1272 (2016).
- [26] K. Ruddick, V. De Cauwer, B. Van Mol, Remote Sens. Coast. Ocean. Environ. **5885**, 588501 (2005).
- [27] G.-S. Chu, Y. Song, X.-C. Li, Y.-M Song, Chinese J. Sci. Instrum. **35**, 138 (2014).
- [28] R. Pasula, Iris recognition in multiple spectral bands: From visible to short wave infrared, PhD thesis, 2011.
- [29] P. -F. Wei, X. -D. Lin, L. Wang, M.-H. Wang, Opt. Prec. Eng. **24**, 1840 (2016).
- [30] H. Sun, D. -J. Wang, T. -X. Ma, W. -C. Xu, Y. Yao, Acta Optica Sinica **37**, 1111002-1 (2017).
- [31] M. Honkanen, V. Kettunen, M. Kuittinen et al., Appl. Phys. B **68**, 81 (1999).
- [32] P. Lalanne, D. Lemerrier-Lalanne, J. Mod. Opt. **43**, 2063 (1996).
- [33] M. G. Moharam, E. B. Grann, D. A. Pommet et al., J. Opt. Soc. Am. A **12**, 1068 (1995).
- [34] D. -J. Wang, H. Sun, X.-Q Sun, Opt. Prec. Eng. **26**, 2371 (2018).

*Corresponding author: lilinear@zju.edu.cn